Journal of Materiomics 6 (2020) 24–32

Contents lists available at ScienceDirect

Journal of Materiomics

journal homepage: www.journals.elsevier.com/journal-of-materiomics/

Intrinsic mechanical behavior of MgAgSb thermoelectric material: An *ab initio* study

Guodong Li [a, b, **], Qi An [c], Umut Aydemir [d, e], Sergey I. Morozov [f], Bo Duan [a], Pengcheng Zhai [a, b, *], Qingjie Zhang [b], William A. Goddard III [g]

[a] Hubei Key Laboratory of Theory and Application of Advanced Materials Mechanics, School of Science, Wuhan University of Technology, Wuhan, 430070, China
[b] State Key Laboratory of Advanced Technology for Materials Synthesis and Processing, Wuhan University of Technology, Wuhan, 430070, China
[c] Department of Chemical and Materials Engineering, University of Nevada Reno, Reno, NV, 89557, USA
[d] Department of Chemistry, Koç University, Sariyer, Istanbul, 34450, Turkey
[e] Boron and Advanced Materials Research Center, Koç University, Sariyer, Istanbul, 34450, Turkey
[f] Department of Computer Simulation and Nanotechnology, South Ural State University, Chelyabinsk, 454080, Russia
[g] Materials and Process Simulation Center, California Institute of Technology, Pasadena, CA, 91125, USA

ARTICLE INFO

Article history:
Received 21 August 2019
Received in revised form
28 October 2019
Accepted 2 November 2019
Available online 7 November 2019

ABSTRACT

α-MgAgSb based thermoelectric (TE) device attracts much attention for its commercial application because it shows an extremely high conversion efficiency of ~8.5% under a temperature difference of 225 K. However, the mechanical behavior of α-MgAgSb is another serious consideration for its engineering applications. Here, we apply density functional theory (DFT) simulations to examine the intrinsic mechanical properties of all three MgAgSb phases, including elastic properties, shear-stress − shear-strain relationships, deformation and failure mechanism under ideal shear and biaxial shear conditions. We find that the ideal shear strength of α-MgAgSb is 3.25 GPa along the most plausible (100)<010> slip system. This strength is higher than that of β-MgAgSb (0.80 GPa) and lower than that of γ-MgAgSb (3.43 GPa). The failure of α-MgAgSb arises from the stretching and breakage of Mg−Sb bond α-MgAgSb under pure shear load, while it arises from the softening of Mg−Ag bond and the breakage of Ag−Sb bond under biaxial shear load. This suggests that the deformation mechanism changes significantly under different loading conditions.

1. Introduction

The rapid industrialization has led to the overexploitation of natural energy such as fossil fuels, which is causing severe environmental issues. Thermoelectric (TE) materials have attracted more and more attention due to their capability of directly converting heat into electricity [1,2]. This eco-friendly energy technology is being considered as one of the potential candidates as an alternative energy source. The conversion efficiency of TE materials can be represented by the dimensionless figure of merit, $zT = \alpha^2\sigma T/\kappa$, where α is Seebeck coefficient, σ is the electrical conductivity, κ is the thermal conductivity, and T is the absolute temperature [3]. In the past two decades, tremendous efforts have been developed to explore new TE materials and to enhance their zT values [4–16]. Bi_2Te_3 based materials with $zT > 1.0$ near room temperature, have been commercially applied in solid state refrigeration [17]. However, low abundancy of Te element on earth largely limits large-scale commercial applications of Bi_2Te_3 based alloys. It is urgent to explore alternative candidates with high TE performance in the low temperature range.

MgAgSb is well known to exist in three phases: low temperature α phase with space group *I*-4*c*2, intermediate temperature β phase with space group *P*4/*nmm*, and high temperature γ phase with space group *F*-43 m. α-MgAgSb based materials, consisting of cheap and abundant elements on earth, were reported as a potential p-

* Corresponding author. Hubei Key Laboratory of Theory and Application of Advanced Materials Mechanics, School of Science, Wuhan University of Technology, Wuhan, 430070, China.
** Corresponding author. Hubei Key Laboratory of Theory and Application of Advanced Materials Mechanics, School of Science, Wuhan University of Technology, Wuhan, 430070, China.
E-mail addresses: guodonglee@whut.edu.cn (G. Li), pczhai@126.com (P. Zhai).
Peer review under responsibility of The Chinese Ceramic Society.

https://doi.org/10.1016/j.jmat.2019.11.002

type high performance TE material in the low temperature range with $zT > 1.0$ [18–24]. Zhu et al. found that the intrinsic weak electron-phonon coupling leads to the high power factor ($\alpha^2\sigma$) of α-MgAgSb, while the three-centered Mg–Ag–Sb bonds in α-MgAgSb can induce low-frequency optical phonons, well explaining the origin of its intrinsic low thermal conductivity [24]. Moreover, various effective doping strategies were used to further improve the zT value of α-MgAgSb [19,21,25–27]. For example, Ren et al. showed that doping with small quantities of Ni can improve the maximum zT to 1.4 [21]. Substitution Mg with Yb can increase strong point-defect phonon scattering, leading to the peak zT of ~1.4 at 550 K [28]. More importantly, MgAgSb based TE devices exhibit a high conversion efficiency of 8.5% under a temperature difference of 225 K, demonstrating a strong prospect for TE applications [18].

In TE applications, TE modulus suffers from cyclic thermal stress, which easily causes cracking or failure of TE materials. Excellent mechanical properties, such as high strength and high toughness, are essential for the reliability of TE devices [29]. Sui et al. reported the macroscopic mechanical properties of α-MgAgSb and found that the nanoindentation hardness, compressive strength, and fracture toughness are 3.3 GPa, 389.6 MPa, and 1.1 MPa $m^{1/2}$, respectively [30]. These mechanical properties of α-MgAgSb are comparable with $CoSb_3$ based TE material, and much stronger than those of other important TE materials such as BiSbTe, PbTe, PbSe, and SnTe, indicating α-MgAgSb is mechanically strong [30]. However, their intrinsic mechanical properties remain unexplored so far.

To determine the intrinsic mechanical behavior of MgAgSb, we applied density functional theory (DFT) simulations to study their structural deformations and failure mechanism responding to the applied pure shear deformation and biaxial shear deformations, respectively. α-MgAgSb is found to have the lowest shear stress along the (100)<010> slip system. While β-MgAgSb and γ-MgAgSb have the lowest shear stress of 0.80 GPa and 3.43 GPa, respectively. Under pure shear load, the stretching and collapse of Mg–Sb substructures dominate the deformation of α-MgAgSb. The formation of Ag–Ag and Mg–Sb bonds strengthens the structural stiffness, and the breakage of Ag–Ag bond leads to the failure of β- MgAgSb. The softening and breakage of Ag–Sb bond result in the failure of γ-MgAgSb. Under biaxial shear (compression + shear) load, the lowest shear stress along the (100)<010> slip system is 1.95 GPa, a decrease of 40% compared with that under pure shear load. In addition, the structural deformation shows that the softening of Mg1–Ag1 bond and breakage of Ag2–Sb1 bond lead to the failure of α-MgAgSb, while the Mg–Sb substructures can hold together. This work explores the intrinsic structure - mechanical property relationships at the atomic scale, which is beneficial for developing reliable MgAgSb based TE devices.

2. Methodology

The intrinsic mechanical properties were performed adopting *ab initio* DFT approach implemented in the VASP code, using the projector augmented wave (PAW) potentials to account for the core-valence interactions [31–33]. The Perdew-Burke-Ernzerhof (PBE) functional was applied to describe the exchange-correlation interaction. The valence electrons for Mg, Ag, Sb were treated as $3s^2$, $4d^{10}5s^1$, and $5s^25p^3$, respectively [34]. For the *ab initio* convergence setup, A 500 eV plane-wave energy cutoff was set to converge force and geometries. Electronic self-consistent field (SCF) and force criterion convergence were set to 1×10^{-6} eV and 1×10^{-2} eV/Å, respectively. The Monkhorst-Pack k-points sampling with a fine resolution of $2\pi \times 1/40$ Å^{-1} was adopted for all *ab initio* simulations. The pure shear and bi-shear mechanical loadings are the same with our previous work on other important TE semiconductors [34–39].

3. Results and discussion

3.1. Crystal structure of α-, β-, and γ-MgAgSb

MgAgSb exhibits three different phases from room temperature to its melting temperature: the room temperature α-phase, the intermediate temperature β-phase, and the high temperature γ-phase.

α-MgAgSb is found to crystalize in tetragonal structure with space group $I\bar{4}2c$, as shown in Fig. 1(a) and (b). The unit cell contains 48 atoms (16 × Mg, 16 × Ag, and 16 × Sb), where Mg and Sb atoms form a distorted Mg–Sb rock-salt substructure with Mg–Sb bond lengths of 2.97–3.03 Å. Ag atom is bonded with Mg and Sb atoms, connecting these distorted Mg–Sb cubes along three axes with Ag–Mg and Ag–Sb bond lengths of ~2.90 and 2.88 Å, respectively. The *ab-initio* determined lattice parameters are $a = 9.28$ and $c = 12.75$ Å, which are only 1.2% and 0.5% larger than the experimental values of $a = 9.18$ and $c = 12.70$ Å at room temperature [22], and agree well with other theoretical predictions of $a = 9.26$ and $c = 12.96$ Å from PBE functional [22].

α-MgAgSb transforms to β-MgAgSb at 330 °C with tetragonal crystal structure as well (space group $P4/nmm$), as shown in Fig. 1(c). It consists of Mg–Sb rock-salt substructures along the *ab* plane, with Ag atoms connecting them along the *c* axis. The structure of β-phase is similar to that of α-phase, but exhibits a higher structural symmetry. The unit cell contains 6 atoms (2 × Mg, 2 × Ag, and 2 × Sb) with Mg–Sb, Ag–Mg, and Ag–Sb bond lengths of ~2.91, 3.02, and 2.95 Å, respectively. The *ab-initio* determined lattice parameters are $a = 4.45$ and $c = 6.88$ Å, which are only 0.7% larger and 0.2% smaller than the experimental values of $a = 4.42$ and $c = 6.89$ Å [22].

γ-MgAgSb forms at 420 °C and is found to be cubic, with space group $F\bar{4}3m$, exhibiting the same structure to half-Heusler materials as shown in Fig. 1(d) [41]. The electropositive Mg and electronegative Sb atoms form a rock-salt type sublattice. The structure consists of 8 Mg–Sb cubic sub-structures, in which 4 Ag atoms are filled and the other four are vacant. The unit cell contains 12 atoms (4 × Mg, 4 × Ag, and 4 × Sb) with Mg–Sb, Ag–Mg, and Ag–Sb bond lengths of 3.28, 2.84, and 2.82 Å, respectively. The *ab-initio* determined lattice parameters are $a = 6.57$ Å, which are only 2.0% smaller than the experimental values of $a = 6.70$ Å [41].

3.2. Elastic properties of α-, β-, and γ-MgAgSb

The elastic properties of α-, β-, and γ-MgAgSb were calculated to understand their structural stability. We investigated the elastic constants (C_{ij}) and then applied the Voigt-Reuss-Hill method [37] to compute Young's moduli (E), bulk modulus (B), shear modulus (G), Poisson ratio (ν), as well as a comparison with previous *ab-initio* and experimental results, as listed in Table 1. Overall, our calculated elastic properties of α-, β-, and γ-MgAgSb agree well with previous *ab initio* and experimental results. However, for α-MgAgSb, our calculated C_{44} and G are about eight and two times larger than previous results [44], respectively. This discrepancy of computing results arises from the different convergence setup. The elastic constants are obtained by calculating the total energy as a function of various cell distortions (δ) from the optimized structure. Different simulation setup, like electronic convergence energy difference, ionic convergence criteria, plane wave cutoff energy, lead to different optimized structure. This will result in different elastic properties. Here, our optimized lattice parameters of α-MgAgSb are $a = 9.28$ and $c = 12.75$ Å, which agree very well with

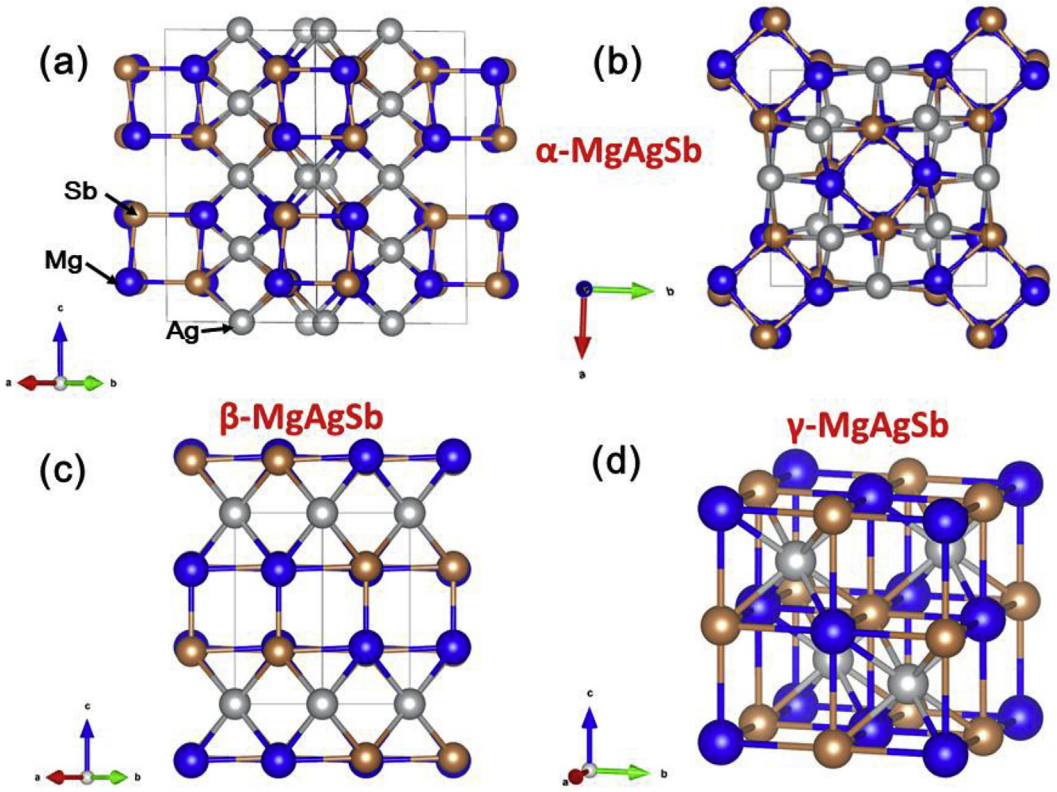

Fig. 1. Crystal structure of MgAgSb. (a) Structure of α-MgAgSb along the [110] direction. (b) Structure of α-MgAgSb in the *ab* plane. (c) Structure of β-MgAgSb along the [110] direction. (d) Structure of γ-MgAgSb.

Table 1
Predicted independent elastic constants (C_{11}, C_{12}, C_{13}, C_{33}, C_{44}) and other related elastic properties: bulk modulus (B), shear modulus (G), Young's modulus (E), Poisson's ratio (v), ductility index (B/G), and hardness (H_v) of α-, β-, and γ-MgAgSb, and the comparison with previous *ab-initio* results. The unit of elastic constants and various moduli is GPa.

Compound	Method	C_{11}	C_{12}	C_{13}	C_{33}	C_{44}	C_{66}	B	G	E	v
α-MgAgSb	Our PBE	86.43	29.91	52.37	67.11	8.92	27.80	56.57	18.52	50.08	0.35
	PBE [44]	89.0	32.9	49.8	69.9	1.1	29.1	56.98	8.08	23.16	0.43
	EXPT [30]									55.0	
	EXPT [24]							43.5			
β-MgAgSb	Our PBE	93.15	20.81	49.99	82.65	7.96	13.69	56.61	15.96	43.76	0.37
	PBE [44]	85.5	25.2	49.7	82.7	3.4	13.9	55.2	8.86	25.22	0.42
γ-MgAgSb	Our PBE	68.97	53.95	53.95	68.97	30.58	30.58	58.72	19.87	53.57	0.35
	PBE [44]	70.6	52.1	52.1	70.6	29.8	29.8	58.3	18.7	50.6	0.36

experimental values of $a = 9.18$ and $c = 12.70$ Å [22], While in the previous *ab initio* studies [44], $a = 9.28$ and $c = 12.80$ Å, suggesting that the c is worse than our simulations. Thus, we believe that the convergence criteria in our work is more reliable than that in Ref. [44].

The elastic mechanical properties (E, B, G) of γ-MgAgSb are much larger than those of α-, and β-MgAgSb, suggesting the structure of γ-MgAgSb is more stable than those of α-, and β-MgAgSb. This agrees well with De long's theoretical calculations exhibiting that γ-MgAgSb has the lowest formation energy [37]. Due to the weak Ag—Sb covalent bonding, the elastic properties of γ-MgAgSb are much lower than those ($B = 128.8$ GPa, $G = 67.2$ GPa, $E = 171.7$ GPa) of strong covalent TiNiSn compound with the same half-Heusler structure [43]. In all three phases, the shear modulus is much lower than the Young's moduli, suggesting shearing failure is much easier to occur compared with tensile failure. Thus, we focus on studying mechanical behaviors of α-, β-, and γ-MgAgSb under shear loading in the next section.

3.3. Intrinsic mechanical deformation behavior of α-, β-, and γ-MgAgSb

3.3.1. Shear-stress – shear-strain relationships

The shear-stress response against shear-strain of an ideal crystal can directly reflect the intrinsic mechanical deformation behavior, including the ideal strength and deformation mechanism [45]. To explore the shear-stress – shear-strain relationships of α-, β-, and γ-MgAgSb, we investigate the pure shear-stress response along different slip systems (Table 2).

Fig. 2 shows the computed shear-stress – shear-strain relationships. In α-MgAgSb, all the shear-stress increases with increasing shear-strain until the maximum stress point. Shearing along the (100)<010> slip system shows a much lower shear-stress compared with those along (001)<100> and (001)<110> systems, representing the (100)<010> system is less rigid in resisting the external shear deformation than the (001)<100> and (001)<110> slip systems. This suggests that the (100)<010> system is the most

Table 2
The selected slip systems of α-, β-, and γ-MgAgSb.

Compound	Slip system	*a, b, c* directions	Supercell	Atoms
α-MgAgSb	(001)<100>	<100>, <010>, <001>	1 × 1 × 1	48
	(001)<110>	<110>, <−110>, <001>	1 × 1 × 1	96
	(100)<010>	<010>, <001>, <100>	1 × 1 × 1	48
β-MgAgSb	(001)<100>	<100>, <010>, <001>	3 × 2 × 3	108
	(001)<110>	<110>, <−110>, <001>	3 × 1 × 3	108
	(100)<010>	<010>, <001>, <100>	3 × 1 × 3	54
γ-MgAgSb	(001)<100>	<100>, <010>, <001>	2 × 1 × 2	48
	(001)<110>	<110>, <−110>, <001>	2 × 1 × 2	96
	(111)<1−10>	<1−10>, <11−2>, <111>	1 × 1 × 1	72

plausible slip system under the same shear stress conditions. Among these systems, (100)<010> has the lowest shear strength of 3.25 GPa at 0.399 shear strain. Beyond this point, the shear-stress suddenly drops to 0.67 GPa at 0.404 shear strain, indicating the bond breakage and structural failure. In β-MgAgSb, with the increasing shear-strain, (100)<010> system processes the weakest resistance against deformation. At 0.209 shear strain, the first maximum shear-stress reaches 0.80 GPa. Then the shear-stress slightly decreases with increasing shear-strain until 0.297 shear strain. Beyond this shear-strain point, the shear-stress rapidly increases with increasing shear-strain. This suggests that the system rearranges to a much stronger structure from 0.209 to 0.297 shear-strain, which leads to the rearranged structure strongly resisting the deformation. At 0.638 shear-strain, the second maximum shear-stress is 3.65 GPa. With further increasing shear-strain to 0.722, the structure is softened and the shear-stress gradually reduces to 3.32 GPa. At fracture strain of 0.731, the shear-stress suddenly drops to 0.28 GPa, representing the bond breakage and the structural collapse. In γ-MgAgSb, (001)<100> and (001)<110> systems show the similar shear-stress responses until 0.166 shear-strain. With the increasing shear-strain, the (001)<110> system further resists the deformation while (001)<100> starts to soften. The (111)<1−10> system is the most likely slip system, exhibiting the lowest shear-stress response with the ideal shear strength of 3.43 GPa. γ-MgAgSb (3.43 GPa) has the largest ideal shear strength compared with α-MgAgSb (3.25 GPa) and β-MgAgSb (0.80 GPa). This agrees well with the trend of their shear modulus ($G_\gamma > G_\alpha > G_\beta$), as listed in Table 1, suggesting γ-MgAgSb is mechanically stronger than α-MgAgSb and β-MgAgSb.

3.3.2. Structural deformation mechanisms

To understand the deformation mechanism, we extracted the structural response against shear strain along their least stress slip systems. Fig. 3 shows the structural patterns of α-MgAgSb along (100)<010> slip system at several critical shear strains. With the shear strain increasing to 0.245, the structure uniformly resists the deformation while all the bond lengths were uniformly deformed (Fig. 3(d)). With the shear strain further increasing to 0.397, the Mg1−Sb1 bond rapidly softens with remarkably increasing bond length, representing the softening of Mg−Sb substructures. This leads to the second shear stress increasing process (Fig. 2(a)). Meanwhile, the Mg2−Sb3 and Mg1−Ag1 bonds were gradually recovered to its original length. The Ag2−Sb2 bond remains nearly unchanged during the shear process. At the fracture strain of 0.404, the Mg1−Sb1 and Mg2−Sb3 bonds rapidly increases to 4.84 and 5.16 Å, respectively, breaking Mg−Sb substructures and relaxing the shear stress, as shown in Fig. 2(a). This stress relaxation leads to the Mg1−Ag1 bond recovery to 2.95 Å, maintaining the well connectivity between these broken Mg−Sb substructures. These typical bond length changes indicate that the stretching and breakage of Mg−Sb substructures dominate the deformation mechanism of α-MgAgSb, while the Ag atoms can well link these Mg−Sb substructures during the whole shear process.

Fig. 4 displays the atomic patterns and typical bonds responses to determine the shear deformation mechanism of β-MgAgSb along the (100)<010> slip system. As the shear strain increases to 0.296, the Mg1−Ag2 and Ag2−Sb1 bonds slightly shrink to accommodate the external deformation (Fig. 4(e)). This leads to gradually increased shear stress until the first maximum stress point (Fig. 2(b)). While the Ag1−Ag2 and Mg2−Sb1 lengths rapidly decrease to 2.93 Å at 0.296 shear strain (Fig. 4(b)), indicating that they are bonded to each other. This new formed bond strengthens the structural stiffness, suppressing stress relaxation (Fig. 2(b)). With further increasing shear strain, the Ag1−Ag2 and Mg2−Sb1 bonds further shrink, strongly resisting the deformation, leading to a remarkably increased shear stress (Fig. 2(b)). The Mg1−Ag2 bond is rapidly stretched and Ag2−Sb1 bond is shrunk until the second maximum stress point (0.60 shear strain). Then, the Ag1−Ag2 and Mg2−Sb1 bond lengths start to increases (Fig. 4(e)). This bond softening leads to the reduced structural stiffness and hence the decreased shear stress (Fig. 2(b)). At 0.722 shear strain, the Mg1−Ag2 bond is stretched to 3.17 Å (Fig. 4(e)), suggesting a softened weak atomic interaction. But the structure still remains good symmetry (Fig. 4(c)). At fracture strain of 0.730, the Ag1−Ag2 length suddenly increases to 3.30 Å, breaking this bond and releasing the shear stress. The Mg2−Sb1 and Mg1−Ag2 bonds recover to 3.02 and 3.03 Å, respectively, releasing the bond deformations. The breakage of Ag1−Ag2 bond collapses the original Mg−Sb framework, deconstructing the structure (Fig. 4(d)).

Fig. 5 displays the atomic configurations and bond-responses of γ-MgAgSb along the least stress slip system of (111)<1−10>. The structure uniformly resists the shear deformation until 0.334 shear strain. While the Mg1−Sb1 bond is gradually shrunk to 2.86 Å (Fig. 5(a,b)). At the fracture strain of 0.346, the Ag1−Sb1 bond length remarkably increases to 4.03 Å, breaking this bond and releasing the shear stress (Fig. 5(c)). The bond responses shown in

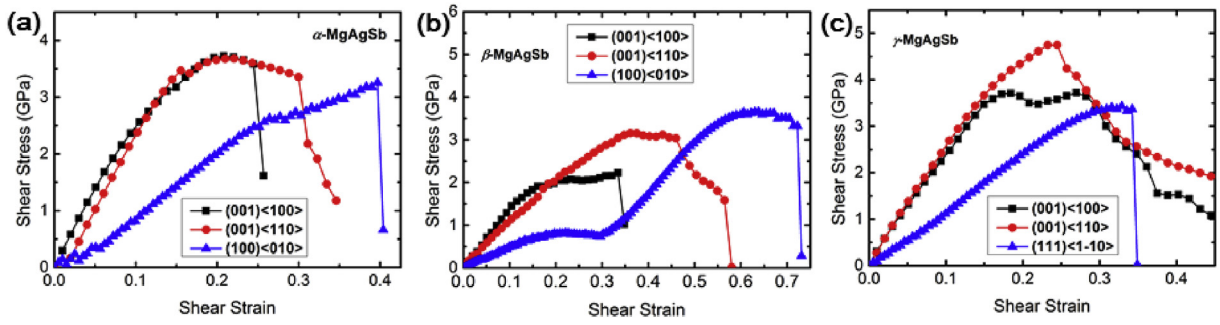

Fig. 2. Shear-stress − shear-strain relationships of (a) α-MgAgSb, (b) β-MgAgSb, and (c) γ-MgAgSb along different directions.

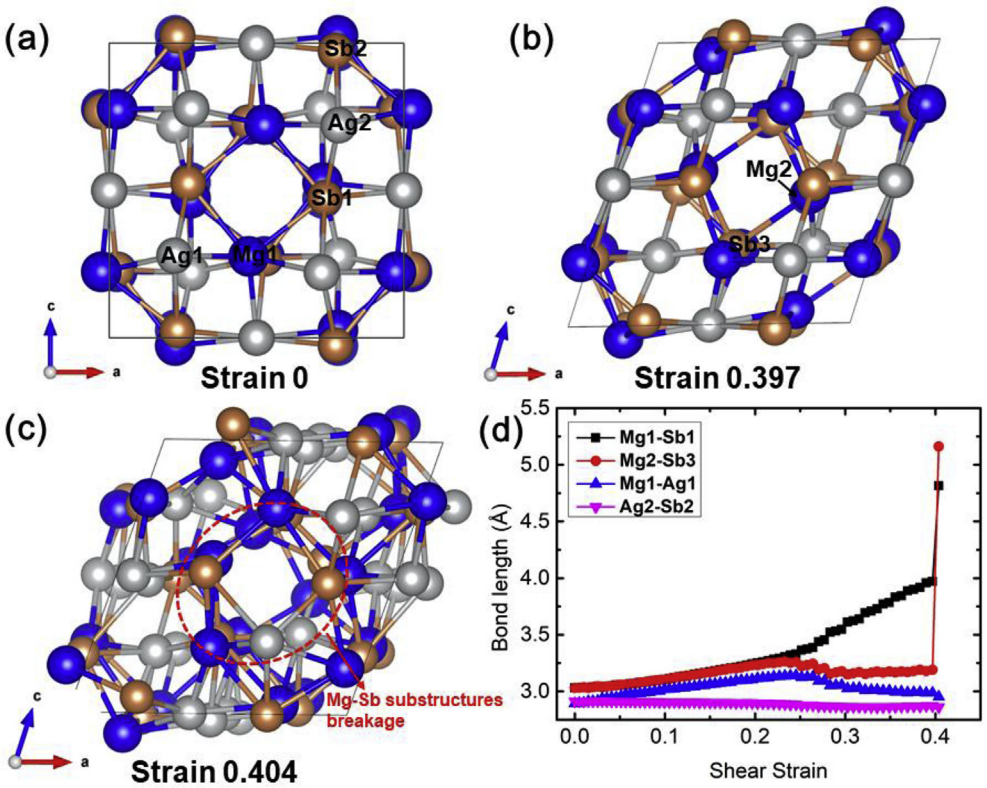

Fig. 3. Structural failure mechanism of α-MgAgSb along (100)<010> slip system at critical shear strains. (a) Atomic structure at 0 shear strain, (b) Atomic structure at 0.397 shear strain corresponding to the ideal shear strength, (c) Atomic structure at 0.404 shear strain corresponding to the structural failure. (d) The typical bond lengths (Mg1–Sb1, Mg2–Sb3, Mg1–Ag1, and Ag2–Sb2) as a function of shear strain.

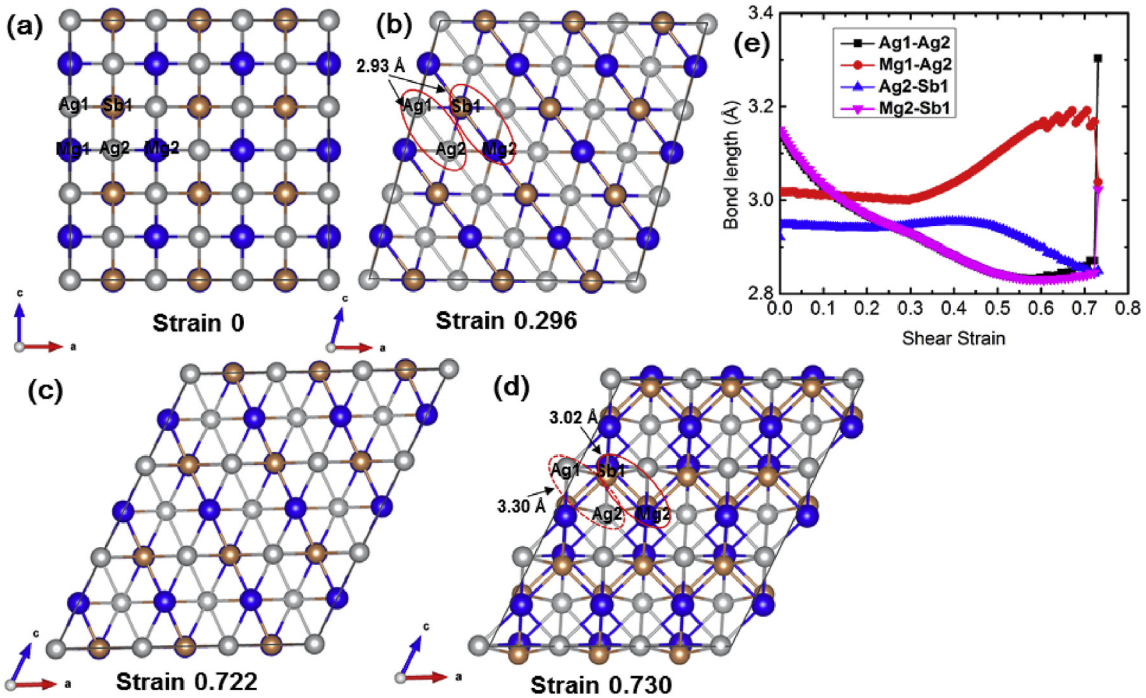

Fig. 4. Structural failure mechanism of β-MgAgSb along least stress slip system of (100)<010> at critical shear strains. (a) Atomic structure at 0 shear strain, (b) Atomic structure at 0.296 shear strain corresponding to the structural rearrangement. (c) Atomic structure at 0.722 shear strain before failure. (d) Atomic structure at fracture strain of 0.730. (e) Typical bond responses (Ag1–Ag2, Mg1–Ag2, Ag2–Sb1, and Mg2–Sb1) against shear strain of β-MgAgSb along the least stress slip system of (100)<010>.

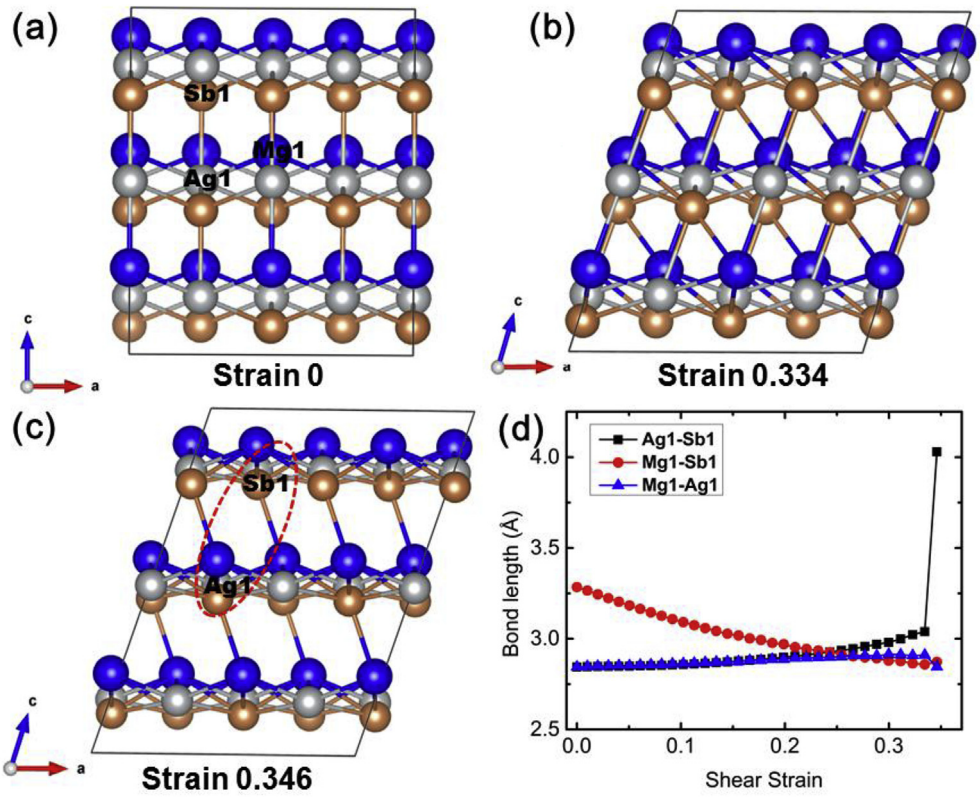

Fig. 5. Structural failure mechanism of γ-MgAgSb along (111)<1–10> slip system at several critical shear strains. (a) Atomic structure at 0 shear strain, (b) Atomic structure at 0.334 shear strain corresponding to the ideal shear strength, (c) Atomic structure at failure strain of 0.346. (d) The typical bond lengths (Ag1–Sb1, Mg1–Sb1, and Mg2–Ag2) as a function of shear strain.

Fig. 5(d) clearly reveal that the Mg1–Sb1 length rapidly reduces with increasing shear strain, which is similar with the Mg1–Sb1 length of β-MgAgSb (Fig. 5). The Ag1–Sb1 and Mg1–Ag1 bond lengths are stretched with the same ratio until 0.2 shear strain. Then, the Ag1–Sb1 bond length increases much faster than the Mg1–Ag1 bond length, suggesting the Ag1–Sb1 bond softens before the Mg1–Ag1 bond. This well explains why the Ag1–Sb1 bond breaks at the fracture strain of 0.346 whereas the Mg1–Ag1 bond recovers to its original length of 2.84 Å (Fig. 5(d)).

3.3.3. *Deformation and failure under indentation stress conditions*

The nano-indentation technology, so called depth-sensing indentation, can measure various mechanical properties of a material at the atomic scale, like load-displacement curve, hardness, fracture toughness, and so on. Therefore, the nano-indentation measurement is important for exploring the nano-mechanical behavior of a material. Here, we applied biaxial shear (shear + compression) deformation to mimic the stress conditions under nano-indentation for understanding the deformation mechanism of α-MgAgSb along the (100)<010> slip system, as shown in Fig. 6(a). As the shear strain increases to 0.161, the stress response under bi-shear load is similar with that under pure shear load. With the increasing shear strain, the stress increases more slowly under bi-shear load (Fig. 6(a)). This indicates that the structural stiffness under bi-shear load is much weaker than that under pure shear load. The maximum shear stress is 1.95 GPa under bi-shear load, a decrease of 40% compared with that (3.25 GPa) under pure shear load. This suggests that compression plays a significant role in the structural deformation at large shear strains. We extracted the structural deformations under bi-shear load, as shown in Fig. 6(b)–(d). With the shear strain increasing to 0.161, the Mg1–Ag1 bond are uniformly stretched, strongly resisting the deformation. While the Mg1–Sb1, Ag1–Sb2, and Ag2–Sb1 bonds nearly remain unchanged. With further increasing shear strain, the Mg1–Ag1 bond length remarkably increases, representing the highly softening of this bond. This well explains why the shear stress changes with a much lower increasing ratio (Fig. 6(a)). The other bonds are still slightly changed, maintaining well structural integrity (Fig. 6(b)). At the fracture strain of 0.308, the Ag2–Sb1 bond sharply increases to 3.55 Å (Fig. 6(d)). The breakage of this bond leads to the structural collapse and stress relaxation (Fig. 6(c)).

Under bi-shear load, the softening of Mg1–Ag1 bond and the breakage of Ag2–Sb1 bond lead to the failure of α-MgAgSb, while the Mg–Sb substructures are not deconstructed. Under the pure shear load, the collapse of Mg–Sb substructures leads to the failure of the α-MgAgSb, while the Mg1–Ag1 and Ag2–Sb1 bonds are not broken (Fig. 3). This biaxial shear simulation reveals that compression along the *c*-axis not only decreases the structural stiffness at large strains, but also changes its failure mechanism of α-MgAgSb.

α-MgAgSb, which has the excellent TE properties, processes the ideal shear strength of 3.25 GPa. This value is much higher than those of van der Waals-like bonding dominated TE materials such as Bi_2Te_3 (0.19 GPa) [38] and SnSe (0.59 GPa) [46], as well as ionic bonding dominated TE materials such as La_3Te_4 (0.99 GPa) [47,48], Mg_3Sb_2 (1.95 GPa) [48] and $CuInTe_2$ (2.43 GPa) [49]. However, α-MgAgSb is much weaker than strong covalent bonding dominated TE materials such as $CoSb_3$ (7.17 GPa) [43] and TiNiSn (10.52 GPa) [41].

Understanding the intrinsic failure mechanism of an ideal single crystal provides the basis for future work to examine the roles of

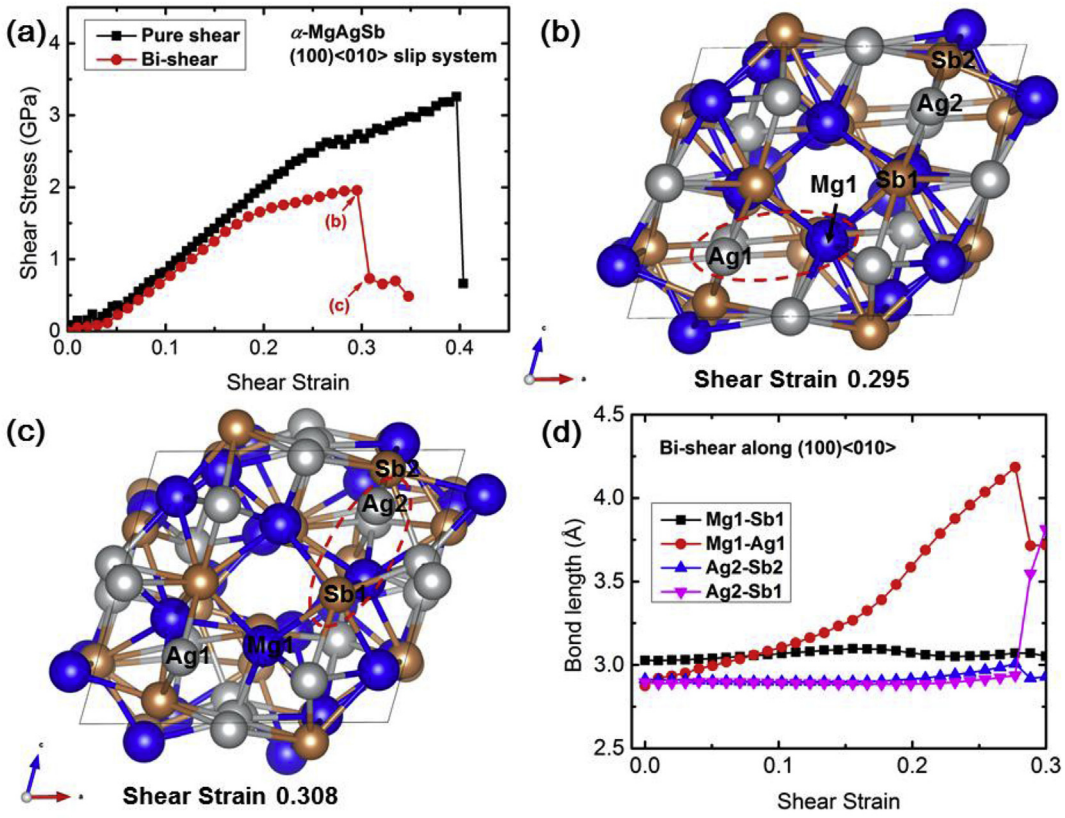

Fig. 6. Biaxial shear deformation of α-MgAgSb along the (100)<010> slip system. (a) The shear-stress – shear-strain relationships under bi-shear and pure shear loads, respectively. (b) Atomic structure at 0.295 shear strain before failure, and (c) Atomic structure at failure strain of 0.308. (d) The typical bond lengths (Mg1–Sb1, Mg1–Ag1, Ag2–Sb2, and Ag2–Sb1) against shear strain.

grain boundaries (GBs) and dislocations in failure process. Our current study on the single crystal is an essential first step for comprehensively understanding the failure of MgAgSb under realistic conditions, which will lay the essential foundation for developing high performance TE materials with excellent mechanical properties.

The mechanical properties of MgAgSb samples are heavily related to such defects as GBs, vacancies and pores that are ubiquitous in real samples. Studying these effects requires much larger systems of millions of atoms. Thus, future studies fitting our DFT results to a force field for molecular dynamics (MD) simulations will be beneficial for studying how such defects influence the mechanical strength. Meanwhile, it is essential to validate our theoretical prediction from mechanical experiments which is beyond the scope of the current work.

4. Conclusions

We performed DFT simulations to investigate the structural and intrinsic mechanical properties of all three MgAgSb phases including elastic modulus, shear-stress – shear-strain relationships, deformation and failure mechanism under ideal shear and indentation stress conditions. The main conclusions include:

- The ideal shear strength of α-MgAgSb is 3.25 GPa along the (100) <010> slip system. This strength is higher than that of β-MgAgSb (0.80 GPa) and lower than that of γ-MgAgSb (3.43 GPa).
- Under ideal shear load, the stretching and collapse of Mg–Sb substructures dominates the deformation of α-MgAgSb.
- The formation of Ag–Ag and Mg–Sb bonds strengthen the structural stiffness and the breakage of Ag–Ag bond leads to the failure of β-MgAgSb under pure shear load.
- The softening and breakage of Ag–Sb bond results in the failure of γ-MgAgSb under ideal shear deformation.
- The biaxial shear simulation reveals that the compression along the *c* axis decreases the lowest shear stress by 40% compared with the ideal shear strength. The structural deformation shows that the softening of Mg1–Ag1 bond and breakage of Ag2–Sb1 bond lead to the failure of α-MgAgSb, while the Mg–Sb substructures are not deconstructed.

Declaration of competing interest

The authors declare that they have no known competing financial interests or personal relationships that could have appeared to influence the work reported in this paper.

Acknowledgements

This work is partially supported by the NSFC (No. 51972253), Fundamental Research Funds for the Central Universities (WUT: 2019IVA055, 2019IB006, 2019III208). S.M. was thankful for the support by Act 211 Government of the Russian Federation, under No. 02.A03.21.0011 and by the Supercomputer Simulation Laboratory of South Ural State University [50].

References

[1] Chang C, Wu M, He D, Pei Y, Wu C, Wu X, Yu H, Zhu F, Wang K, Chen Y,

Huang L, Li J, He J, Zhao L. 3D charge and 2D phonon transports leading to high out-of-plane ZT in n-type SnSe crystals. Science 2018;360:778.
[2] He J, Tritt TM. Advances in thermoelectric materials research: looking back and moving forward. Science 2017;357.
[3] Snyder GJ, Toberer ES. Complex thermoelectric materials. Nat Mater 2008;7:105.
[4] Wang T, Zhao K, Qiu P, Song Q, Chen L, Shi X. Aguilarite Ag4SSe thermoelectric material: natural mineral with low lattice thermal conductivity. ACS Appl Mater Interfacesfaces 2019;11:12632.
[5] Zhu H, He R, Mao J, Zhu Q, Li C, Sun J, Ren W, Wang Y, Liu Z, Tang Z, Sotnikov A, Wang Z, Broido D, Singh DJ, Chen G, Nielsch K, Ren Z. Discovery of ZrCoBi based half Heuslers with high thermoelectric conversion efficiency. Nat Commun 2018;9.
[6] Guan M, Zhao K, Qiu P, Ren D, Shi X, Chen L. Enhanced thermoelectric performance of quaternary Cu2-2xAg2xSe1-xSx liquid-like chalcogenides. ACS Appl Mater Interfaces 2019;11:13433.
[7] Luo Z, Hao S, Cai S, Bailey TP, Tan G, Luo Y, Spanopoulos I, Uher C, Wolverton C, Dravid VP, Yan Q, Kanatzidis MG. Enhancement of thermoelectric performance for n-type PbS through synergy of gap state and fermi level pinning. J Am Chem Soc 2019;141:6403.
[8] Zheng Y, Liu C, Miao L, Li C, Huang R, Gao J, Wang X, Chen J, Zhou Y, Nishibori E. Extraordinary thermoelectric performance in MgAgSb alloy with ultralow thermal conductivity. Nano Energy 2019;59:311.
[9] Jin M, Lin S, Li W, Chen Z, Li R, Wang X, Chen Y, Pei Y. Fabrication and thermoelectric properties of single-crystal argyrodite Ag8SnSe6. Chem Mater 2019;31:2603.
[10] Liu Y, Fu C, Xia K, Yu J, Zhao X, Pan H, Felser C, Zhu T. Lanthanide contraction as a design factor for high-performance half-heusler thermoelectric materials. Adv Mater 2018;30.
[11] Zhou J, Zhu H, Liu T, Song Q, He R, Mao J, Liu Z, Ren W, Liao B, Singh DJ, Ren Z, Chen G. Large thermoelectric power factor from crystal symmetry-protected non-bonding orbital in half-Heuslers. Nat Commun 2018;9.
[12] Hanus R, Agne MT, Rettie AJE, Chen Z, Tan G, Chung DY, Kanatzidis MG, Pei Y, Voorhees PW, Snyder GJ. Lattice softening significantly reduces thermal conductivity and leads to high thermoelectric efficiency. Adv Mater 2019:e1900108. Deerfield Beach, Fla.
[13] Zeuthen CM, Thorup PS, Roth N, Iversen BB. Reconciling crystallographic and physical property measurements on thermoelectric lead sulphide. J Am Chem Soc 2019;141:8146–57.
[14] Anand S, Xia K, Zhu T, Wolverton C, Snyder GJ. Temperature dependent n-type self doping in nominally 19-electron half-heusler thermoelectric materials. Adv Energy Mater 2018;8.
[15] Xin J, Yang J, Li S, Basit A, Sun B, Li S, Long Q, Li X, Chen Y, Jiang Q. Thermoelectric performance of rapidly microwave-synthesized alpha-MgAgSb with SnTe nanoinclusions. Chem Mater 2019;31:2421.
[16] Zhang A, Zhang B, Lu W, Xie D, Ou H, Han X, Dai J, Lu X, Han G, Wang G, Zhou X. Twin engineering in solution-synthesized nonstoichiometric Cu5FeS4 icosahedral nanoparticles for enhanced thermoelectric performance. Adv Funct Mater 2018;28.
[17] Zheng Y, Zhang Q, Su X, Xie H, Shu S, Chen T, Tan G, Yan Y, Tang X, Uher C, Snyder GJ. Mechanically robust BiSbTe alloys with superior thermoelectric performance: a case study of stable hierarchical nanostructured thermoelectric materials. Adv Energy Mater 2015;5.
[18] Liu Z, Mao J, Sui J, Ren Z. High thermoelectric performance of alpha-MgAgSb for power generation. Energy Environ Sci 2018;11:23.
[19] Liu Z, Geng H, Mao J, Shuai J, He R, Wang C, Cai W, Sui J, Ren Z. Understanding and manipulating the intrinsic point defect in alpha-MgAgSb for higher thermoelectric performance. J Mater Chem 2016;4:16834.
[20] Ying P, Liu X, Fu C, Yue X, Xie H, Zhao X, Zhang W, Zhu T. High performance alpha-MgAgSb thermoelectric materials for low temperature power generation. Chem Mater 2015;27:909.
[21] Zhao H, Sui J, Tang Z, Lan Y, Jie Q, Kraemer D, McEnaney K, Guloy A, Chen G, Ren Z. High thermoelectric performance of MgAgSb-based materials. Nano Energy 2014;7:97.
[22] Kirkham MJ, Dos Santos AM, Rawn CJ, Lara-Curzio E, Sharp JW, Thompson AJ. Ab initio determination of crystal structures of the thermoelectric material MgAgSb. Phys Rev B 2012;85.
[23] Mi J, Ying P, Sist M, Reardon H, Zhang P, Zhu T, Zhao X, Iversen BB. Elaborating the crystal structures of MgAgSb thermoelectric compound: polymorphs and atomic disorders. Chem Mater 2017;29:6378.
[24] Ying P, Li X, Wang Y, Yang J, Fu C, Zhang W, Zhao X, Zhu T. Hierarchical chemical bonds contributing to the intrinsically low thermal conductivity in α-MgAgSb thermoelectric materials. Adv Funct Mater 2017;27:1604145.
[25] Tan X, Wang L, Shao H, Yue S, Xu J, Liu G, Jiang H, Jiang J. Improving thermoelectric performance of α-MgAgSb by theoretical band engineering design. Adv Energy Mater 2017;7:1700076.
[26] Liu Z, Wang Y, Mao J, Geng H, Shuai J, Wang Y, He R, Cai W, Sui J, Ren Z. Lithium doping to enhance thermoelectric performance of MgAgSb with weak electron-phonon coupling. Adv Energy Mater 2016;6:1502269.
[27] Miao N, Zhou J, Sa B, Xu B, Sun Z. Pressure-induced semimetal-semiconductor transition and enhancement of thermoelectric performance inα -MgAgSb. Appl Phys Lett 2016;108:213902.
[28] Liu Z, Zhang Y, Mao J, Gao W, Wang Y, Shuai J, Cai W, Sui J, Ren Z. The microscopic origin of low thermal conductivity for enhanced thermoelectric performance of Yb doped MgAgSb. Acta Mater 2017;128:227.
[29] Barako MT, Park W, Marconnet AM, Asheghi M, Goodson KE. Thermal cycling, mechanical degradation, and the effective figure of merit of a thermoelectric module. J Electron Mater 2013;42:372.
[30] Liu Z, Gao W, Meng X, Li X, Mao J, Wang Y, Shuai J, Cai W, Ren Z, Sui J. Mechanical properties of nanostructured thermoelectric materials α-MgAgSb. Scripta Mater 2017;127:72.
[31] Kresse DJ G. From ultrasoft pseudopotentials to the projector augmented-wave method. Phys Rev B 1999;3:1758.
[32] Kresse G, Furthmüller J. Efficiency of ab-initio total energy calculations for metals and semiconductors using a plane-wave basis set. Comp Mater Sci 1996;6:15.
[33] Kresse G, Furthmüller J. Efficient iterative schemes for ab initio total-energy calculations using a plane-wave basis set. Phys Rev B Condens Matter 1996;54:11169.
[34] Perdew JP, Burke K, Ernzerhof M. Generalized gradient approximation made simple. Phys Rev Lett 1996;77:3865.
[35] Li G, An Q, Morozov SI, Duan B, Goddard WAI, Zhai P, Zhang Q, Snyder GJ. Mechanical softening of thermoelectric semiconductor Mg2Si from nano-twinning. Scripta Mater 2018;157:90.
[36] Li G, An Q, Morozov SI, Duan B, Goddard WAI, Zhang Q, Zhai P, Snyder GJ. Ductile deformation mechanism in semiconductor alpha-Ag2S. NPJ Comput Mater 2018;4.
[37] Li G, Aydemir U, Morozov SI, Miller SA, An Q, Goddard WAI, Zhai P, Zhang Q, Snyder GJ. Mechanical properties in thermoelectric oxides: ideal strength, deformation mechanism, and fracture toughness. Acta Mater 2018;149:341.
[38] Li G, Aydemir U, Morozov SI, Wood M, An Q, Zhai P, Zhang Q, Goddard WAI, Snyder GJ. Superstrengthening Bi2Te3 through nanotwinning. Phys Rev Lett 2017;119.
[39] Li G, Morozov SI, Zhang Q, An Q, Zhai P, Snyder GJ. Enhanced strength through nanotwinning in the thermoelectric semiconductor InSb. Phys Rev Lett 2017;119.
[41] Li G, An Q, Aydemir U, Goddard WAI, Wood M, Zhai P, Zhang Q, Snyder GJ. Enhanced ideal strength of thermoelectric half-Heusler TiNiSn by sub-structure engineering. J Mater Chem 2016;4:14625.
[43] Li G, An Q, Li W, Goddard WAI, Zhai P, Zhang Q, Snyder GJ. Brittle failure mechanism in thermoelectric skutterudite CoSb3. Chem Mater 2015;27:6329.
[44] Wang J, Fu X, Zhang X, Wang J, Li X. Structural, elastic, electronic, and thermodynamic properties of MgAgSb investigated by density functional theory. Chin Phys B 2016;25:291.
[45] Ogata S, Li J, Yip S. Ideal pure shear strength of aluminum and copper. Science 2002;298:807.
[46] Li G, Aydemir U, Wood M, Goddard WA, Zhai P, Zhang Q, Snyder GJ. Ideal strength and deformation mechanism in high-efficiency thermoelectric SnSe. Chem Mater 2017;29:2382.
[47] Li G, Aydemir U, Wood M, Goddard WAI, Zhai P, Zhang Q, Snyder GJ. Mechanical properties of thermoelectric lanthanum telluride from quantum mechanics. J Phys D Appl Phys 2017;50.
[48] Li G, Aydemir U, Wood M, An Q, Goddard WA, Zhai P, Zhang Q, Snyder GJ. Deformation mechanisms in high-efficiency thermoelectric layered Zintl compounds. J Mater Chem 2017;5:9050.
[49] Li G, An Q, Morozov SI, Duan B, Zhai P, Zhang Q, Goddard III WA, Snyder GJ. Determining ideal strength and failure mechanism of thermoelectric CuInTe2 through quantum mechanics. J Mater Chem 2018;6:11743.
[50] Kostenetskiy PS, Safonov AY. SUSU supercomputer resources. Proceedings of the 10th annual international scientific conference on parallel computing technologies. 2016. Arkhangelsk, Russia.

Dr. Guodong Li is a Professor of Hubei Key Laboratory of Theory and Application of Advanced Materials Mechanics, Wuhan University of Technology (WUT). He obtained the doctor degree from Wuhan University of Technology in 2013. Then he studied in California Institute of Technology and Northwestern University from 2014 to 2018 as a postdoctoral scholar. He joined WUT as a professor from 2019. His research interests mainly focus on micro- and nano- mechanical behavior of thermoelectric materials, multi-scale theoretical simulations, defect chemistry, and so on.

Dr. Pengcheng Zhai a Professor of the State Key Laboratory of Advanced Technology for Materials Synthesis and Processing at WUT, and dean of School of Science at WUT. He received his Ph.D. degree from WUT in 1998. His current research interests include theoretical calculations of transport properties and mechanical failure of thermoelectric materials, theoretical modeling of heat transport properties of thermoelectric modules, thermoelectric bulk materials and the related application technology.